Energy dependence of interference phenomena in the forward-scattering regime of photoelectron diffraction

Sylvain Tricot, Thomas Jaouen, D. Sébilleau, Philippe Schieffer

Energy dependence of interference phenomena in the forward-scattering regime of photoelectron diffraction

S. Tricot[a], T. Jaouen[a], D. Sébilleau[a], P. Schieffer[a]

[a] *Univ Rennes, CNRS, IPR (Institut de Physique de Rennes) - UMR 6251, F-35000, Rennes, France*

Abstract

X-ray photoelectron diffraction is a powerful spectroscopic technique in the direct legacy of C. S. Fadley that combines high sensitivity to the arrangement of atoms in crystals and element specificity providing unique fingerprints of selected atomic sites in matter. When used with kinetic energies between 500 eV and 1500 eV, its interpretation and description is based on the fact that the atomic scattering factors are strongly forward-peaked in such a way that low-angles scattering and backscattering events are respectively dominant and almost irrelevant in the photoemission process. In this paper we aim to demonstrate with the help of multiple-scattering simulations that energy scans of high-energy (500-1500 eV) forward-scattering photoelectron diffraction can provide valuable structural and chemical information about thin epitaxial films or stacking of two-dimensional materials.

Keywords: X-ray photoelectron diffraction, forward scattering, energy-scan, high-order interference

1. Introduction

Angle-resolved photoemission of electrons from near-surface atoms of solid crystals with kinetic energies ranging from 500 eV to 1500 eV provides efficient, element-specific, structural information about local atomic structures such as lattice parameters, composition and reconstruction of surfaces and interfaces, and adsorbate geometries (1; 2; 3; 4; 5). In this particular kinetic energy regime of the so-called X-ray Photoelectron Diffraction (XPD) technique, forward focusing effects indeed dominate the electron-atom scattering amplitudes in such a way that the photoemission intensity shows zero-order interference enhancements at emission angles corresponding to dense atomic directions (2). Among the plenty of pioneering works carried out by C. S. Fadley in the field of photoemission, the development of the theoretical description of high-energy forward scattering (FS) XPD has taken a very special place throughout his career. That story begun by his first use of XPS FS to determine the internuclear axis or orientation of bonds of CO adsorbed on transition metal surfaces (6; 7) and continued over the years through his constant implication for the improvement of the simulation and interpretation of XPD for bulk- and surface-atomic structures using multiple-scattering methods (8).

In general, whether in the FS regime of XPD, in low-energy backscattering studies (<500 eV) (9), or in hard X-ray photoelectron spectroscopy in which photoelectron diffraction patterns are dominated by Kikuchi bands (5-20 keV) (10), it is essential to perform multiple-scattering (MS) calculations and to vary the structural parameters for optimizing the theory-experiment agreement (11; 12) and extracting the maximum amount of structural information. Such approach has been previously demonstrated to be highly powerful in so-called angle-resolved photoemission extended fine structure studies (13), that focused on energy scans of backscattering at low photoelectron kinetic energies (9) for accessing the geometry of molecules, atoms or monolayers on crystal surfaces. We aim, in this paper, to demonstrate through MS calculations that in the high-energy (500-1500 eV) FS regime of photoelectron diffraction, the little-explored energy-scan data collection mode can specifically provide valuable structural and chemical information about thin epitaxial films or stacking of two-dimensional materials.

In the high-energy FS regime, fine structures related to high-order interferences between various scattering paths can combine to FS-related intensity enhancements in the angle scans ultimately leading to a *breakdown of the forward scattering behavior* characterized by intensity depressions instead of enhancements along the dense atomic directions (14). We will specifically address the energy dependence of these interference phenomena in the FS regime of photoelectron diffraction. Through MS calculations performed on Si(001), a benchmark crystal in solid-state physics, we will demonstrate that exploiting interference phenomena in FS energy scans allow to solve tiny changes of atomic structures with an extremely high sensitivity at the sub-Å length scale.

2. Computational details

The multiple scattering spherical wave cluster calculations have been performed in the Rehr-Albers framework (15) by using the MsSpec program (16; 17; 18). The phase shifts have been calculated by using a complex Hedin-Lundqvist exchange and correlation potential (19; 20; 21) whose imaginary part is able to describe the finite electron mean free path in the final state, with a muffin-tin radius of 1.1 Å. Polar (θ) and azimuth (ϕ) angles are defined with respect to the normal and to the

(100) emission plane of the (001) cluster surface, respectively. At angles $\theta = 0°$ and $\phi = 0°$, the photon source defines an angle of 54.7° with respect to the surface normal aligned with the analyzer direction. Lattice vibrations were described by averaging over T-matrix elements and using isotropic mean-square displacements (MSD). For simulations done at room temperature (RT), the MSD was 6×10^{-3} Å^2. We systematically applied MSD values 20% larger for the surface atoms as they vibrate more than the bulk ones. The Rehr-Albers truncation order which controls the degree of sphericity introduced in the description of the basis functions used to expand the wave function around each atomic center was set to 2 for the Si 2s level. It is consistent with the rule of thumb given by the Fadley group (22) according to which the truncation order is well approximated by $l_i + 1$, where l_i is the angular momentum of the excited core state. The number of scattering paths to take into account in computing the final cross-section can dramatically increase when considering a large number of atoms and for large scattering orders. To avoid wasting computational resources in calculating scattering paths that weakly contribute to the final signal, we filtered out paths whose total lengths were longer than 30 Å (corresponding to 1.5-2 electron mean free path) and whose angles of any scattering events, except the last one, were greater than 40° or 60°.

Since we focus on high-energy FS regime of XPD, the effect of the deviations from bulk geometry of atoms located in the surface region is small (23), so that we consider bulk-terminated surfaces. To model the signal of a *full substrate*, a spherical cluster is built with a radius of 20 Å, truncated at the surface and one plane below the emitter's plane. The full signal is the sum of diffraction patterns computed for emitters in all planes from the surface plane down to the 15$^{\text{th}}$ plane beneath the surface. This cluster shape allows to achieve MS calculations for relatively deep planes while keeping a reasonable number of atoms in the cluster (980 atoms). To model *thin films*, the same method as above was used but with a hemispherical cluster 15 Å in radius containing 363 atoms (9 planes).

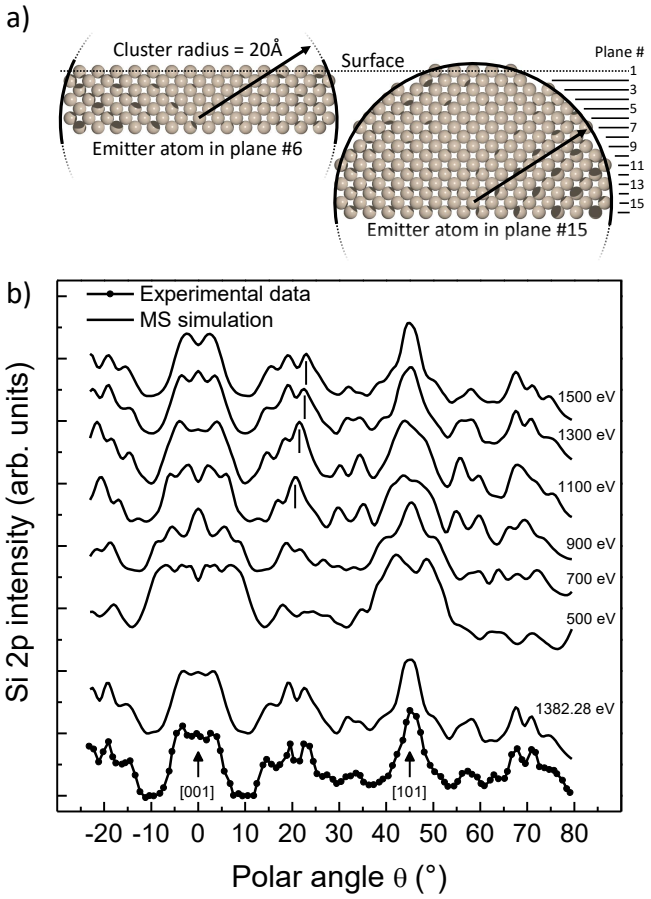

Figure 1: a) Side view of the cluster used to compute the full diffraction diagrams shown in (b) for planes 6 and 15. Complete calculations are done for emitters in planes 1 to 15. The shape of each cluster is spherical and truncated at the surface. Planes deeper than the plane below the emitter are not taken into account. b) Multiple scattering (MS) simulations up to scattering order 5 of XPD polar scans of the Si 2p core level for a Si(001) substrate in the (100) emission plane for selected photoelectron kinetic energies between 500 eV and 1500 eV (full lines). The lower curve at 1382.28 eV can be compared to the experimental data taken from Ref. (24) (symbol + line). The curves are normalized such as the main structure that spreads over 10-15° around normal emission are normalized to [0, 1]. The curves are shifted in intensity for the sake of readability. Vertical dashes in the upper MS simulated polar scans are a guide to the eye of the energy shift of the high-order interferences-related fine structures around 20° of polar angle.

3. Results and discussion

3.1. Energy-dependence of Si 2p XPD polar scans: Experiment vs. MS calculations

In order to demonstrate how powerful MS calculations are for accurately describing both the intensity and shape of FS peaks in XPD polar scans, we first show, in Figure 1, a comparison between a high-resolution experimental XPD polar scan of the Si 2p core level of a Si(001) substrate recorded in the (100) emission plane [bottom curve with dotted symbols, Fig.1b)] and MS calculations performed at 1382.28 eV of kinetic energy [simulated bottom curve in full line, Fig.1b)]. Examples of the clusters used to compute the theoretical polar scans are shown in Fig. 1a) for emitter atoms in the 6$^{\text{th}}$ (left hand-side) and 15$^{\text{th}}$ planes (right-hand side) below the surface. The complete calculation was done for emitters in planes 1 to 15. The shape of each cluster was chosen to be spherical and truncated at the surface and planes deeper than one plane below the emitter were not considered. The multiple-scattering expansion of the photoelectron wave function was carried out up to the fifth order which we checked to be sufficient to achieve convergence. The Rehr-Albers truncation order was set to 2 and its value was decremented by 1 after each scattering event. In the excitation process, only the $p \rightarrow d$ channel was considered since the radial matrix element for the $p \rightarrow s$ channel is much smaller and can be dropped out to speed up the calculation. Paths with a scattering angle larger than 40° after a diffusion event were not considered. The calculations have been averaged over 49 directions filling a cone of 1° half-angle. The MSD of the bulk Si atoms have been fixed to the RT value of 6×10^{-3} Å^2 (25), and those of the surface atoms considered to be enhanced by a factor of 1.2. The experimental polar scan has been extracted

from Ref. (24) and was acquired on hydrogen-terminated (001) p-type Si samples using a Physical Electronics 5400 XPS system. An angle resolution down to 1° was obtained by adjusting the entrance slit of the analyzer. Non-monochromatic Al Kα X-ray (1486.6 eV of photon energy) was used for excitation, and the incident light defined a fixed angle of 54.7° with respect to the analyzer direction. As we can see, the agreement between the experimental polar scan and the MS-calculated one is remarkable. The positions, shapes and relative intensities of the various structures are very well reproduced. As expected in a forward focusing regime, the photoemission intensity shows, in a first approximation, enhancements along the [001] and [101] directions of the Si lattice. The intensity modulations between 0° and 45° of polar angles are nevertheless not only related to FS along dense atomic directions. In particular, we notice rather fine structures around 20° of polar angle [marked by the vertical dashes Fig.1b)], that gradually shift as the kinetic energy increases from 500 eV to 1500 eV within our theoretical XPD polar scans [full lines, Fig.1b)]. This behavior, together with characteristic small amplitudes and widths (of the order of a few degrees), is typical of high-order interferences of the emitted and scattered electronic waves.

The energy dependence of the photoemission intensity along the [001] and [101] atomic directions then shows that high-order interferences fine structures are ubiquitous and combine to FS-related intensity enhancements. The most pronounced effect concerns the XPD peak along the [001] direction that shows, in both the experimental and the simulated XPD diagrams, high interferences-related fine structures at +/-3° and a strong dependence on the kinetic energy of its shape exhibiting the well-known *volcano shape* at 500 eV, 900 eV, 1100 eV and 1500 eV of kinetic energies. This peculiar shape has been previously observed in other systems such as SiC, MgO, and GaN systems and has been shown to be induced by close neighboring atoms via inter-chain processes and to mainly depend on their scattering potentials and on the energy at which the scattering takes place (26; 27; 28). In the following, we will demonstrate that thanks to high angle resolutions as currently provided by most of photoemission set-up in synchrotron facilities, we can access detailed structural information of ultra-thin layers by finely analyzing the energy dependence of interference phenomena acting on *normal-emission* FS peaks in so-called energy scans. Indeed, focusing on energy-scans of the normal-emission FS peak instead of large-polar angles ones (>30°), presents the great advantages to be much less affected by the apparatus function and angle averaging effects induced by possible mosaic twists of the overlayer crystallites resulting from the epitaxial growth process (29).

3.2. *Calculated energy-scan of the Si(001) normal-emission FS peak*

Let us now focus on the kinetic-energy dependence of a full XPD diagram around normal emission calculated for a Si cluster of 9 atomic planes representative of a Si(001) thin film of 1.1 nm in thickness. The MS calculations have been performed for photoelectron emission from the 2s orbital of Si rather than

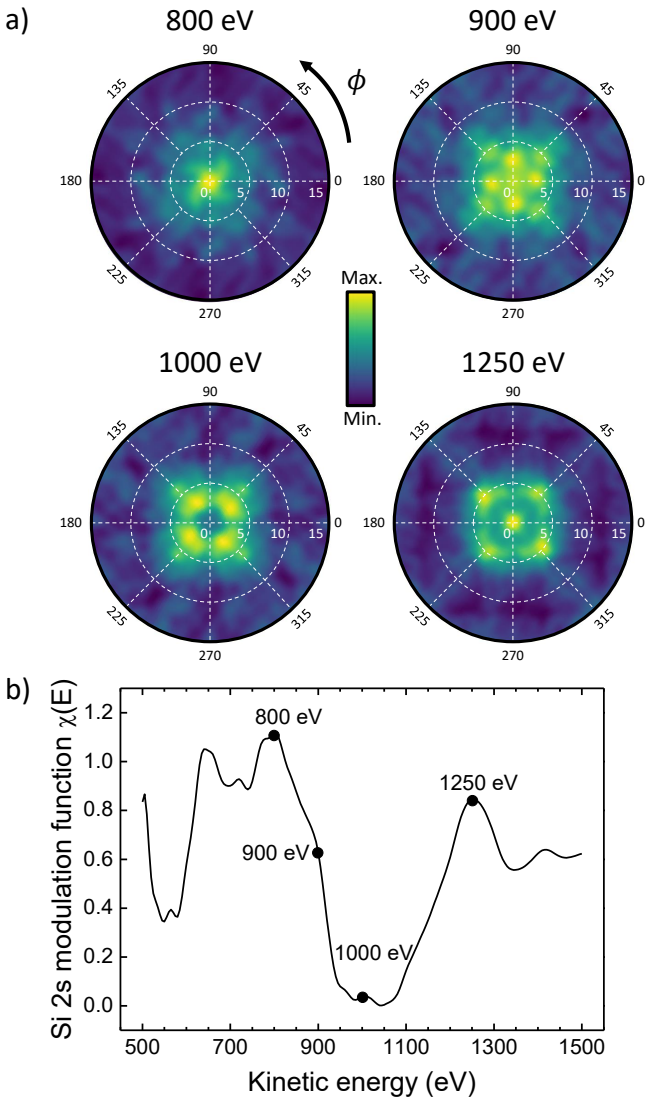

Figure 2: a) Stereographic projections of the Si 2s photoemission intensity for photoelectron kinetic energies of 800, 900, 1000 and 1250 eV, for polar angles θ between 0° and 15°, and for azimuth angles ϕ ranging from 0° to 360°. The (100) emission plane corresponds to ϕ=0°. The reported intensity corresponds to the modulation function of Eq. 1. The intensity distribution exhibits large variations especially at the normal emission. b) Si 2s normal-emission modulation function as a function of the kinetic energy. The dots represent the energy points of the stereographic projections of a).

from the 2p one since it allows to significantly reduce the computational time without affecting the drawn conclusions. Scattering paths containing deflections by more than 60° after a scattering event were not taken into account in this calculation. Figure 2a) shows stereographic projections of (θ, ϕ) MS calculations performed up to the fourth scattering order for the 2s core level of Si at 4 selected kinetic energies in the FS regime of photodiffraction and with polar angles between normal emission and 15°. No experimental averaging was taken into account at this stage and the MSD of the bulk and surface Si atoms have been fixed to the RT values of 6×10^{-3} Å^2 and 7.2×10^{-3} Å^2, respectively. As observed for the Si substrate, the

normal-emission XPD structure strongly depends on the kinetic energy of the photoelectrons. Around 800 eV and 1250 eV, it consists of a peak of ∼1° wide, whereas at ∼ 900 eV and ∼1000 eV, a depression surrounded by a ring of enhanced intensity at polar angles of 3° appears, forming the so-called volcano shape. To get a systematic view of the energy dependence of the interference phenomena acting on the normal-emission FS peak, we plot in Fig. 2b) the modulation function $\chi(E)$ of the Si 2*s* cross-section as a function of the kinetic energy (E), in the whole FS regime. The modulation function $\chi(E)$ is defined by:

$$\chi(E) = \frac{I_0(E) - I_{0,direct}(E)}{I_{0,direct}(E)}, \quad (1)$$

where $I_0(E)$ and $I_{0,direct}$ are respectively the calculated, total and direct (diffraction-free), normal photoemission intensities at a given kinetic energy E. Interestingly, the modulation function $\chi(E)$ shows an overall oscillating behavior over a long-energy range reflecting interference phenomena between scattering paths at short-length scale in real-space. It especially shows strong variations between maxima values of ∼1.2 close to 800 eV and less than 0.1 around 1000 eV where almost no diffraction-induced intensity enhancement occurs. Superimposed to such a large amplitude and long-period oscillation, it exhibits, throughout the energy-scan, successive local maxima which reflect constructive and destructive interferences at larger length scales, similar to what has already been observed in the backscattering energy range of photodiffraction (100-400 eV) (9). Note that, whereas the low-energy region of XPD is usually dedicated to the study of adsorption of molecules on surfaces due to the favored 180° scattering and the rather small mean-free path, in our case, the relevant scattering paths being mainly due to FS or scattering with small angles <90°, energy scans of high-energy photoelectron diffraction are particularly well suited for probing the structural properties of thin epitaxial films or stacking of two-dimensional materials.

3.3. Origin of the long-period oscillating behavior in the normal-emission FS energy scan.

In order to get some insight on the nature of the short-length scale interference phenomena responsible for the large amplitude and long-period oscillating behavior in the normal-emission FS energy scan, we performed single scattering calculations over various simplified Si clusters in which atoms have been removed and looked for the involved scattering paths. Figure 3a) shows the calculated modulation function of the Si 2*s* normal-emission FS peak for a 5 atoms cluster. Obviously, the local maxima reflecting the long-range interferences are not tracked by our calculations, but, interestingly, the long-period oscillating behavior is already perfectly reproduced, with maxima at 714 eV and 1454 eV and a minimum at 1043 eV. Figure 3b) (left hand-side) shows the stereographic projections of the Si 2*s* intensity at these selected kinetic energies calculated within the single-scattering approximation for polar angles between normal emission and 60° and an azimuth angle-range of 360°. We identify forward scattering peaks along the [101], [$\bar{1}$01], [011] and [0$\bar{1}$1] directions surrounding by intensity ripples which correspond to high-order interferences with scatter-

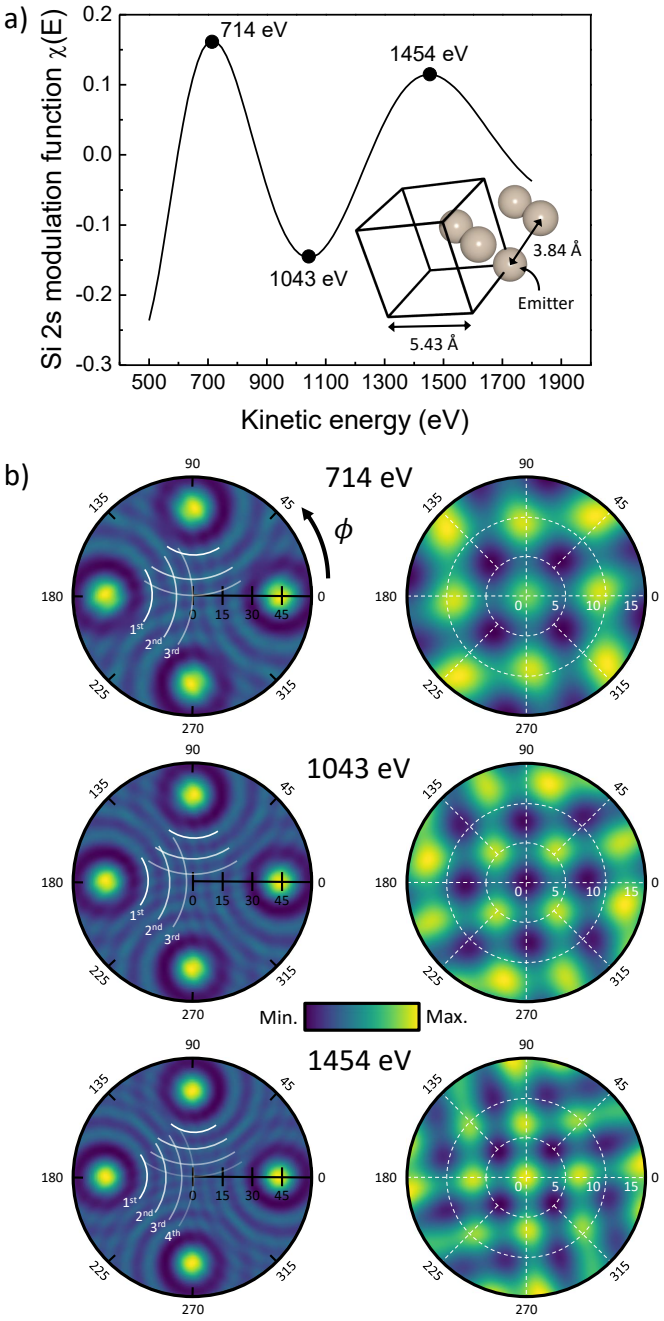

Figure 3: a) Single-scattering calculations of the Si 2*s* normal-emission intensity as a function of the kinetic energy. The inset shows the 5 atoms cluster used for the simulation. Long-energy range oscillations of the modulation function are well reproduced by this small subset of atoms. The dots mark the kinetic energies at which the stereographic projections of b) have been calculated. b) Left: stereographic projections of the Si 2*s* intensity calculated within the single-scattering approximation for photoelectron kinetic energies of 714 eV, 1043 eV and 1454 eV (from top to bottom). Polar angles vary between normal emission and 60° and azimuth lies in the [0°, 360°] range. Right: same as left but for polar angles between normal emission and 15°. Wavefronts are highlighted with white lines in the left panel of b) as a guide to the eye to identify the different interference orders leading to constructive or destructive intensity at normal emission (right panel).

ing angles of 45°. Looking at more closely between 0° and 15° of polar angles [Fig. 3b), right-hand side], we effectively see that intensity maxima are present at normal emission for 714 eV and 1454 eV of kinetic energy whereas at 1043 eV, we recognize the volcano shape. From these simulations, we can thus conclude that the maxima/minimum of the modulation function at 714 eV (1454 eV)/1043 eV partly originates from third and fourth orders constructive/destructive interferences between electronic waves scattered once by each of the four surrounding atoms [see white lines in the left panel of Fig. 3b)]. It is interesting to note that the normal-emission intensity modulation reflects the combined effect of 4 scattering atoms that are located relatively close to the emitting atom [second-nearest neighbors in the bulk Si(001) lattice] at a moderated scattering angle of ~45°. The additional fact that the modulus of the scattering factor at this scattering angle is still significant, when compared to the normal-emission one, finally explains the enhancement of the interference effects in the [001] high-symmetry direction.

3.4. Impact of angle-resolution and temperature on normal-emission FS energy-scans.

We now discuss the experimental requirements in terms of angle-resolution and temperature for accessing the maximum amount of structural information from the interference phenomena in the normal-emission FS energy scans. Focusing, first, on the impact of the finite size of the analyzer entrance hole on the intrinsic angle averaging of the measurement, we performed MS calculations of the Si 2*s* normal-emission modulation function as a function of the kinetic energy for half-angles of the detector acceptance cone ranging from 0° to 3.5° therefore simulating ultimate to low angle resolutions [Fig. 4a)]. As we can see, the modulation function shows a continuous amplitude decrease as the acceptance angle increases and does not show a strong dependence on kinetic energy anymore for angles higher than 3.5 °. This reflects through the disappearance of the high-order interference features in polar diagrams that only consist of FS-related intensity enhancements along the [001] and [101] and [111] atomic directions (results not shown). We also notice, in Fig. 4a), that even though the long-period oscillating behavior is rather robust with respect to the loss of angle-resolution, the local maxima at 650 eV, 790 eV and 1250 eV reflecting the long-range interferences already disappear for angles higher than 1.5°. This demonstrates that further prospects of exploiting the energy-dependence of interference phenomena in the FS regime of XPD requires angle-resolution better than 1.5°. Note that, with their angle-resolutions of tenths or even hundredths of degrees, the current two-dimensional, deflection-based hemispherical, or time-of-flight electron analyzers (30), now largely permit to perform energy-scan FS XPD with ultimate angle *and* energy resolutions on modern synchrotron facilities.

Another intrinsic mechanism of angle averaging in XPD comes from scattering of photoelectrons with vibrating atoms at finite temperature. To take into account the effect of such thermal vibrations, we varied, in our MS calculations, the amplitude of the uncorrelated and isotropic atomic motions described by

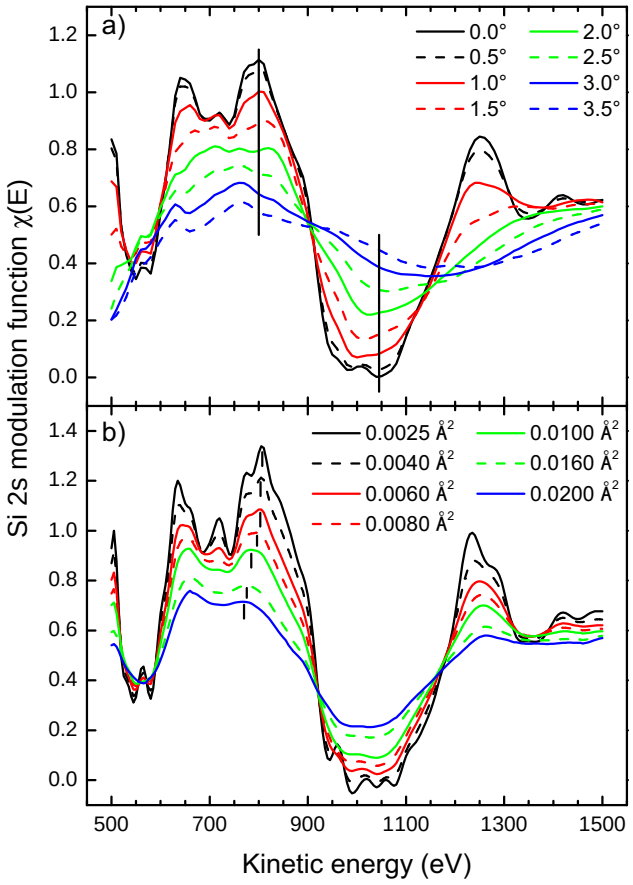

Figure 4: a) Si 2*s* normal-emission modulation function as a function of the kinetic energy for different half-angles of the detector acceptance cone simulating ultimate (0°) to low (3.5°) angle resolutions. Even though long-range oscillations may still be visible at low resolution, fine structure features disappear above 1.5° or 2°. b) Same as a) but for different atoms MSD corresponding to temperatures of 0 K, 168 K, 282 K, 396 K, 511 K, 853 K and 1082 K. The acceptance of the analyzer is kept constant with an acceptance cone of 0.5° half-angle.

the MSD. All calculations presented so far were performed using the experimental RT value for the bulk Si atoms and considering enhanced MSD at the surface (1.2 factor as compared to the bulk). We now consider the temperature dependence of the MSD that shows a quasi-constant value of 2.5×10^{-3} Å^2 below 50 K, and non-linear and linear variations with a slope of 1.75×10^{-5} Å^2/K, between 50 K and 150 K, and above 150 K, respectively (25). Figure 4b) shows the energy-scans of the normal-emission Si 2*s* modulation function for selected values of the Si MSD (the corresponding lattice temperatures are given in the caption) for a 9 atomic-planes cluster. The calculations were performed up to scattering order 4 with an analyzer acceptance cone of 0.5° half-angle and for a constant Si lattice parameter of 5.43 Å . At the lowest temperature, the modulation function shows a large number of high-order interferences-related fine structures [see vertical dashes on Fig. 4b)]. As the temperature increases, the amplitude of the modulation function decreases, the finest structures progressively dis-

appear, and only the long-period oscillating behavior remains at the highest temperatures. The modulation amplitude decreases by only 20% between 0 K and 282 K demonstrating that the lattice vibrations have only a minor effect on the FS energy-scans, in agreement with the experimental polar scans that show that high-order interference effects around the normal-emission FS peak can be readily observed at RT for a Si(001) surface given a high angle resolution [half angle < 1.5°] (24; 26; 27; 28).

3.5. Sensitivity of normal-emission FS energy-scans to lattice deformations.

In this last section, we aim to conclude by illustrating how sensitive the normal-emission FS energy scans can be to tiny changes of lattice parameters and atomic structures as induced by strain. Here again, we focus on the energy-dependence of the normal-emission Si 2*s* modulation function computed for the 9 atomic-planes Si(001) cluster with an analyzer acceptance cone of 0.5° half-angle and bulk and surfaces MSD values similar to those used in the first two subsections. As for Figure 4, these simulations correspond to scattering order 4 and scattering events included in a 60° half-angle cone. Figure 5a) shows the energy dependencies of normal-emission Si 2*s* modulation functions for lattice parameters, a_0, of 5.43 Å , 5.33 Å , and 5.53 Å , corresponding to the true atomic structure of Si(001) at 300 K and to compressed and expanded lattices with relative variations of the lattice parameter, $\Delta a_0/a_0$, of ±1.84%. Remarkably, the normal-emission FS energy-scan shows an extremely high sensitivity to such a small change in lattice parameter. Although its shape and amplitude are rather independent of a_0, it shows energy-offsets, over large energy-scales, towards lower or higher kinetic energies depending on the positive or negative sign of $\Delta a_0/a_0$ and that depend on the kinetic energy, the offsets being larger for higher energies. In order to quantify the high-sensitivity of the normal-emission FS energy-scan to changes in lattice parameters, we introduce the parameter $S_{lp}(E)$ defined as:

$$S_{lp}(E) = \frac{\Delta\chi(E)}{\Delta a_0}, \tag{2}$$

where $\Delta\chi(E)$ is the variation of the modulation function at the kinetic energy E induced by a change Δa_0 in the lattice parameter. Doing so for our Si(001) example, we find a maximum sensitivity of -4.1/Å at 900-910 eV of kinetic energy [see the vertical arrow in the Fig. 5a)]. Considering that, from an experimental point, modulation function variations $\Delta\chi(E)$ of ±0.1 can be measured, the proposed method of energy-scanning normal-emission FS peaks should allow to access lattice parameters changes as small as ~ ±0.03 Å .

Figure 5b) finally illustrates the sensitivity of normal-emission FS energy-scans to in-plane biaxial lattice strains, as introduced during epitaxy for example. To this end, we compare the energy-dependence of the Si 2*s* normal-emission modulation function computed using the Si(001) lattice parameter a_0 of 5.43 Å to those calculated for thin films under tensile or compressive strains, therefore exhibiting in-plane biaxial deformations ϵ of ±1.0%. Both films are assumed to be uniformly strained and to be subject to tetragonalization of the Si lattice

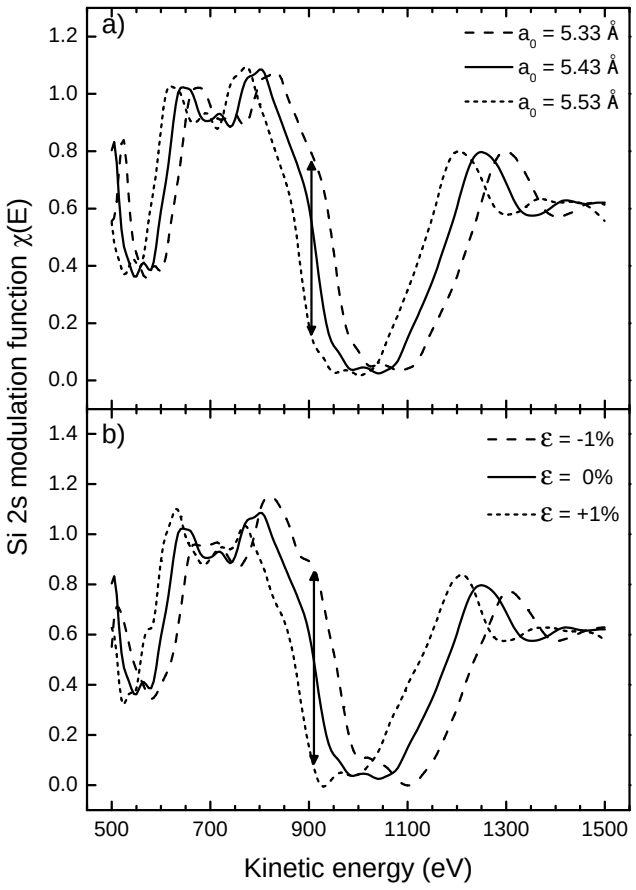

Figure 5: a) Si 2*s* normal-emission modulation function as a function of the kinetic energy for Si(001) lattice parameters a_0 of 5.43 Å and ±0.1 Å around this value. b) Same as a) but for in-plane biaxial tensile or compressive strains of 1% of the cubic cell. Both a) and b) show that energy scans in the 500-1500 eV range may provide an extremely high sensitivity to tiny structural changes.

as calculated within the linear elasticity model using a Poisson coefficient of 0.28. As we could have expected, the impact of strain on the normal-emission FS energy-scan is very similar to that of the lattice parameter previously discussed. Here also, the strain leaves almost unchanged the shape and amplitude of the energy variations of the modulation functions, but introduces energy-offsets whose magnitude depends on both kinetic energies and ϵ and whose direction depends on the sign of the latter, solely [compressive (tensile) strains corresponding to negative (positive) energy-shifts]. In the same way as before, we introduce the parameter $S_{strain}(E)$ for quantifying the sensitivity of the normal-emission FS energy-scan to strain. It is defined by:

$$S_{strain}(E) = \frac{\Delta\chi(E)}{\epsilon}, \tag{3}$$

where $\Delta\chi(E)$ is the variation of the modulation function at the kinetic energy E induced by a slight film deformation ϵ of ±0.25 %. In that case, we also find a huge sensitivity of normal-emission FS energy-scans to strain with a maximum sensitivity of ~-48 at ~910-920 eV of kinetic energy [see the vertical arrow in the Fig. 5b)] that corresponds to lattice deformations of

the order of ±0.2 % considering accessible modulation function variations $\Delta\chi(E)$ of ±0.1.

4. Conclusion

In this paper, through MS calculations performed on a benchmark crystal, we have theoretically addressed the energy dependence of interference phenomena in the specific FS regime of photoelectron diffraction. We have shown that for a proper description of a normal-emission XPD peak measured with a high-angle resolution, both the usual FS-related zero-order and high-order interferences phenomena have to be taken into account. The latter being strongly dependent on kinetic energy, energy-scanning normal-emission XPD peaks in the FS regime gives rise to very-marked oscillations of the modulation function of the photoemission intensity that we demonstrated to be extremely sensitive to tiny changes of the crystal lattice therefore providing a highly powerful spectroscopic probe of atomic structures of ultrathin films and two-dimensional heterostructures. We believe that our study, in direct lineage of the C.S. Fadley legacy, may provide a new tool to the still very active XPD community. Indeed, given the high angle and energy resolutions as well as the broad tunable photon energy provided by most of photoemission set-up in modern synchrotron facilities, they should motivate further experimental prospects of exploiting normal-emission FS energy scans.

References

[1] C. S. Fadley, The Study of Surface Structures by Photoelectron Diffraction and Auger Electron Diffraction, Springer US, Boston, MA, 1992, p. 421.

[2] W. F. Egelhoff Jr., X-Ray photoelectron and auger electron forward scattering: A new tool for surface crystallography, Critical Reviews in Solid State and Materials Sciences 16 (1990) 213.

[3] S. A. Chambers, Epitaxial film crystallography by high-energy Auger and X-ray photoelectron diffraction, Advances in Physics 40 (1991) 357.

[4] D. P. Woodruff, A. M. Bradshaw, Adsorbate structure determination on surfaces using photoelectron diffraction, Reports on Progress in Physics 57 (1994) 1029.

[5] P. Schieffer, A. Guivarc'h, C. Lallaizon, B. Lépine, D. Sébilleau, P. Turban, G. Jézéquel, Formation of a body-centered-cubic Fe-based alloy at the Fe/GaAs(001) interface, Applied Physics Letters 89 (2006) 161923.

[6] L. G. Petersson, S. Kono, N. F. T. Hall, C. S. Fadley, J. B. Pendry, Determination of Adsorbate Geometries from Intramolecular Scattering in Deep-Core-Level X-Ray Photoemission: CO on Ni(001), Phys. Rev. Lett. 42 (1979) 1545.

[7] C. S. Fadley, S. Kono, L.-G. Petersson, S. Goldberg, N. Hall, J. Lloyd, Z. Hussain, Determination of surface geometries from angular distributions of deep-core-level X-ray photoelectrons, Surf. Sci. 89 (1979) 52.

[8] D. Sébilleau, K. Hatada, H. Ebert, Multiple Scattering Theory for Spectroscopies, Springer Proceedings in Physics 204 (2018).

[9] D. Phil Woodruff, Photoelectron diffraction: Early demonstrations and alternative modes, Journal of Vacuum Science & Technology A 39 (4) (2021) 040801.

[10] A. Winkelmann, C. S. Fadley, F. J. G. de Abajo, High-energy photoelectron diffraction: model calculations and future possibilities, New Journal of Physics 10 (2008) 113002.

[11] T. Jaouen, S. Tricot, G. Delhaye, B. Lépine, D. Sébilleau, G. Jézéquel, P. Schieffer, Layer-Resolved Study of Mg Atom Incorporation at the MgO/Ag(001) Buried Interface, Phys. Rev. Lett. 111 (2013) 027601.

[12] T. Jaouen, P. Aebi, S. Tricot, G. Delhaye, B. Lépine, D. Sébilleau, G. Jézéquel, P. Schieffer, Induced work function changes at Mg-doped MgO/Ag(001) interfaces: Combined Auger electron diffraction and density functional study, Phys. Rev. B 90 (2014) 125433.

[13] J. J. Barton, S. W. Robey, D. A. Shirley, Theory of angle-resolved photoemission extended fine structure, Phys. Rev. B 34 (1986) 778.

[14] A. Chassé, L. Niebergall, P. Rennert, I. Uhlig, T. Chassé, Breakdown of the forward scattering model in MgO(001), Surface Review and Letters 6 (1999) 1207.

[15] J. J. Rehr, R. C. Albers, Scattering-matrix formulation of curved-wave multiple-scattering theory: Application to x-ray-absorption fine structure, Phys. Rev. B 41 (1990) 8139.

[16] D. Sébilleau, R. Gunnella, Z.-Y. Wu, S. D. Matteo, C. R. Natoli, Multiple-scattering approach with complex potential in the interpretation of electron and photon spectroscopies, Journal of Physics: Condensed Matter 18 (2006) R175.

[17] D. Sébilleau, C. Natoli, G. M. Gavaza, H. Zhao, F. Da Pieve, K. Hatada, MsSpec-1.0: A multiple scattering package for electron spectroscopies in material science, Computer Physics Communications 182 (2011) 2567.

[18] S. Tricot, D. Sebilleau, *MsSpec package*, Python version.

[19] L. Hedin, S. Lundqvist, Effects of Electron-Electron and Electron-Phonon Interactions on the One-Electron States of Solids, Vol. 23, Academic Press, United States, 1969, pp. 1–181.

[20] L. Hedin, B. I. Lundqvist, Explicit local exchange-correlation potentials, Journal of Physics C: Solid State Physics 4 (1971) 2064.

[21] T. Fujikawa, K. Hatada, L. Hedin, Self-consistent optical potential for atoms in solids at intermediate and high energies, Phys. Rev. B 62 (2000) 5387.

[22] Y. Chen, F. J. García de Abajo, A. Chassé, R. X. Ynzunza, A. P. Kaduwela, M. A. Van Hove, C. S. Fadley, Convergence and reliability of the Rehr-Albers formalism in multiple-scattering calculations of photoelectron diffraction, Physical Review B 58 (19) 13121–13131.

[23] G. Gewinner, U. Kafader, P. Wetzel, C. Pirri, X-ray photoelectron diffraction from Si(111): short versus longer range structural sensitivity, Journal of Electron Spectroscopy and Related Phenomena 67 (3) (1994) 387.

[24] T. Katayama, H. Yamamoto, M. Ikeno, Y. Mashiko, S. Kawazu, M. Umeno, Elimination of X-Ray Photoelectron Diffraction Effect of on Si(100) for Accurate Determination of on SiO_2 Overlayer Thickness, Japanese Journal of Applied Physics 38 (1999) L770.

[25] A. Mazur, J. Pollmann, Anisotropy of the mean-square displacements at the Si(001) – (2×1) surface, Surface Science 225 (1990) 72.

[26] D. Agliz, A. Quémerais, D. Sébilleau, Splitting effects in high resolution and high energy photoelectron diffraction: the case of MgO(001), Surface Science 343 (1995) 80.

[27] S. Juillaguet, L. Kubler, M. Diani, J. Bischoff, G. Gewinner, P. Wetzel, N. Bécourt, Strong element dependence of C 1s and Si 2p X-ray photoelectron diffraction profiles for identical C and Si local geometries in $\beta-$-SiC, Surface Science 339 (1995) 363.

[28] P. Schieffer, G. Jézéquel, B. Lépine, D. Sébilleau, G. Feuillet, B. Daudin, X-ray photoelectron diffraction from cubic GaN(001): an experimental and theoretical study, Surface Science 482-485 (2001) 593–599.

[29] R. Chierchia, T. Böttcher, H. Heinke, S. Einfeldt, S. Figge, D. Hommel, Microstructure of heteroepitaxial GaN revealed by x-ray diffraction, Journal of Applied Physics 93 (2003) 8918.

[30] A. K. R. Ang, Y. Fukatsu, K. Kimura, Y. Yamamoto, T. Yonezawa, H. Nitta, A. Fleurence, S. Yamamoto, I. Matsuda, Y. Yamada-Takamura, K. Hayashi, Time-resolved X-ray photoelectron diffraction using an angle-resolved time-of-flight electron analyzer, Japanese Journal of Applied Physics 59 (2020) 100902.